3D-printed CuNi alloy catalyst with triply periodic minimal surface for reverse water-gas shift reaction

Wenbin Li,[#a,d] Junhao Ding,[#b] Xiao Chen,[c] You Wang,[d] Xu Song*[b] and Sai Zhang*[a,d]

[a] Research & Development Institute of Northwestern Polytechnical University in Shenzhen, 518057 Shenzhen, China

[b] Department of Mechanical and Automation Engineering, Chinese University of Hong Kong, Shatin, 999077 Hong Kong, China

[c] School of Materials Science and Engineering, North China University of Water Resources and Electric Power, Zhengzhou 450045, China

[d] School of Chemistry and Chemical Engineering, Northwestern Polytechnical University, 710072 Xian, China

[#] These authors contributed equally: Wenbin Li, Junhao Ding

Email: zhangsai1112@nwpu.edu.cn and xsong@mae.cuhk.edu.hk

Experimental Section

Geometric modelling and 3D printing

The honeycomb was modelled using the CAD software SOLIDWORKS 2020, while Triply Periodic Minimal Surfaces (TPMS)-based lattice structures were modelled *via* implicit functions using MATLAB R2020a.[1] Both were exported in the stereolithography (STL) format for printing. Subsequently, the commercial software Materialise Magics was employed to conduct slicing, toolpath planning, and machine code generation.

$$\Phi_D(x,y,z) = \sin(\omega x)\sin(\omega y)\sin(\omega z) + \cos(\omega x)\sin(\omega y)\sin(\omega z) + \sin(\omega$$

Where $\omega = 2\pi/l$, and l bears the physical meaning of a single cell length, c is a constant value which controls the location of the middle surface with a zeros distance field value.

The printing was conducted by a selective laser melting machine, Han's Laser M100μ, equipped with a CW fibre laser ($\lambda = 1070$ nm) with a fine beam spot size of 25 μm. Regarding the processing parameters, the laser power, scanning speed, layer thickness, and hatch distance were 70 W, 600 mm/s, 10 μm, and 50 μm, respectively. Nitrogen was used to provide a protective atmosphere and ensure an oxygen content of <500 ppm.

Materials

Nickel nitrate hexahydrate ($Ni(NO_3)_2 \cdot 6H_2O$), copper nitrate trihydrate ($Cu(NO_3)_2 \cdot 3H_2O$), and aluminium oxide (Al_2O_3) were obtained from energy and chemical industries. All reagents were of analytical grade and were used directly

without further purification.

Synthesis of the CuNi/Al$_2$O$_3$ catalysts

The CuNi/Al$_2$O$_3$ catalysts were prepared using a traditional impregnation method. Firstly, 300 mg of the commercial Al$_2$O$_3$ supports was dispersed in 35 mL of ethanol. Then, 5 mL of Ni(NO$_3$)$_2$·6H$_2$O and Cu(NO$_3$)$_2$·3H$_2$O solutions containing 4.5 mg of Cu and 4.5 mg of Ni were added to the suspension of the Al$_2$O$_3$ supports. After stirring for 1 h at room temperature, the mixture was volatilised at 60 °C to yield the CuNi/Al$_2$O$_3$ catalysts.

Characterization

The surface quality of the printed samples was measured based on the depth reconstruction using an RH-200 high-resolution 3D optical microscope. The powder X-ray diffraction (XRD) patterns of the catalysts were recorded using a Bruker D8 DISCOVER A25 X-ray diffractometer (Germany) with Co Kα radiation (3 kV). Morphological images and elemental compositions of the catalysts were obtained using scanning electron microscopy (SEM) and energy-dispersive X-ray spectroscopy (EDS), respectively. Transmission electron microscopy (TEM) was performed using a JEOL2100F instrument with an accelerating voltage of 200 kV. High-angle annular dark-field scanning transmission electron microscopy (HAADF-STEM) and elemental mapping analyses were performed using an FEI Tecnai F30 microscope operating at 300 kV. XPS profiles were acquired from a Thermo Electron Model K-Alpha with Al Ka as the excitation source.

Numerical Simulation

To better understand the velocity field distribution inside the catalysts with different geometries during the reaction, computational fluid dynamics (CFD) analysis was conducted using Ansys Fluent 21.0 software. The fluid flow in the catalyst was assumed to be steady-state turbulent flow with a shear stress transport (SST) k–ω model. The entire heat transfer process is governed by the continuity, energy, and momentum equations.

Catalytic tests of catalysts

The RWGS was performed in a fixed-bed reactor at atmospheric pressure. The specific experimental steps are as follows.

Various monolithic catalysts were added to a straight quartz tube with temperature sensors inside and outside the tube. Before the reaction, the catalysts were pre-reduced for 2 h with H_2/CO_2 (75%, 20 mL min^{-1}) at 450 °C. After cooling to room temperature, an H_2/CO_2 gas mixture (25 vol% CO_2 and 75 vol% H_2) was introduced into the reactor at a total flow rate of 20 mL min^{-1}. The gas products were analysed online using a gas chromatograph (North Point GC 901A) equipped with a TCD and a flame ionisation detector (FID).

The conversion of CO_2 was calculated as

$$Conv.CO_2 = \frac{CO_{2in} - CO_{2out}}{CO_{2in}} \times 100\% \quad .$$

The CO and CH_4 selectivity were calculated as

$$Sel.CO = \frac{CO_{out}}{CO_{2in} - CO_{2out}} \times 100\% \quad ,$$

$$Sel.CH_{4=}\frac{CH_{4out}}{CO_{2in} - CO_{2out}} \times 100\%$$.

The yield of CO was calculated as

$$Yield\ of\ CO = Conv.CO_2 \times Sel.CO ,$$

where CO_{2in}, CO_{2out}, CO_{out}, and CH_{4out} represent the moles of CO_2, CO, and CH_4 in the effluent.

Test of exposed active sites

CO chemical pulse adsorption tests were performed on the catalyst using an Auto Chem 2920 chemisorption instrument (Mac Company, United States) equipped with a thermal conductivity detector (TCD).

CO chemical pulse adsorption test: Firstly, load the DL2-RD20 catalyst into the sample tube, and then pretreat it in a 10% H_2/Ar atmosphere at 450 °C for 1 hour to ensure the activation of the exposed metal sites and the removal of adsorbed impurities. Then, reduce the temperature to 50 °C and inject a quantitative amount of CO at a stable helium flow rate. When the response value of CO does not change with the number of pulses, it means that the adsorption reaches saturation. The number of exposed metal sites is determined based on the saturation adsorption value of CO.

The same methods were used to confirm the amount of active sites in the CuNi/Al_2O_3 catalysts.

Mechanical testing

Hot compression tests were performed on a universal test machine, SANS CMT5150, with a constant nominal strain rate of 10^{-3} s^{-1}. The compression temperatures were set as 25, 100, 300 and 400 °C, respectively. The yield stress was

evaluated from the engineering stress–strain curve with a plastic strain offset of 0.2%.

The plateau stress was calculated using the following equation:

$$\sigma_p = \frac{\int_0^{\varepsilon_d} \sigma(\varepsilon)d\varepsilon}{\varepsilon_d},$$

where the ε_d is the densification strain, and $\sigma(\varepsilon)$ is the engineering stress at the strain of ε.

Calculation of reaction equilibrium

The gas-phase thermochemical data of reactants at different temperatures were found from NIST Chemistry Webbook. According to the equation of the RWGS reaction, and H and S of reactants and products at different temperatures, ΔH and ΔS of the equation were calculated. Then, the thermodynamic state function ΔG was calculated based on ΔH and ΔS, and the formula $\Delta G = \Delta H - T \times \Delta S$ was used. The reaction equilibrium constant (K) was calculated as
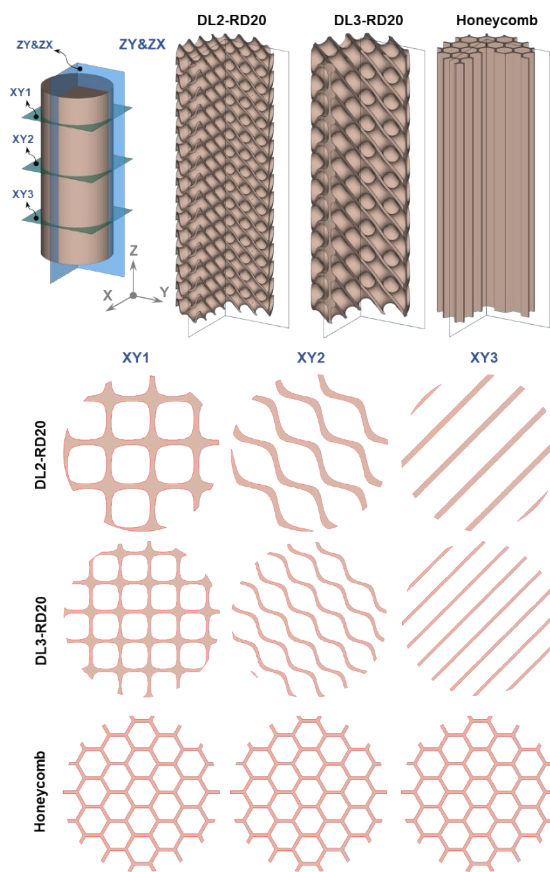
$$\Delta G = -RT\ln K,$$

where R is the gas constant and T is the absolute temperature.

The chemical equilibrium at each temperature was calculated based on the ratio of hydrogen to carbon dioxide ($H_2:CO_2 =3:1$) under the reaction conditions. The specific equation is
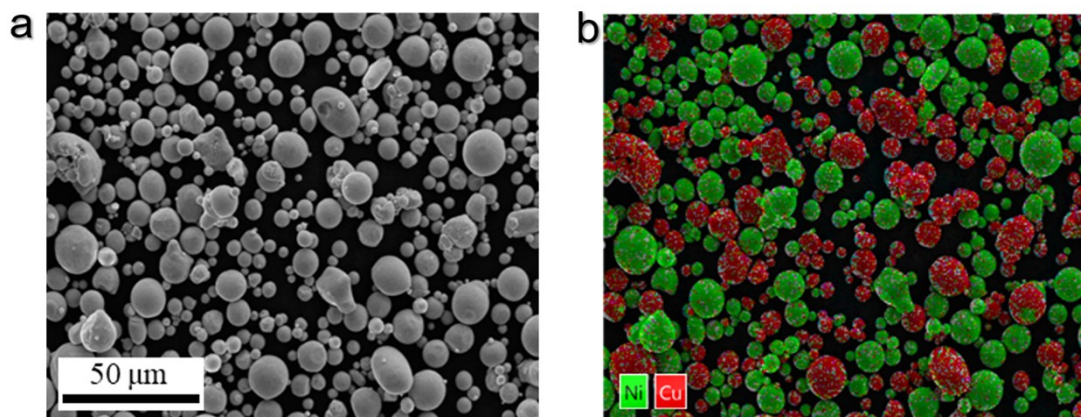
$$K = \frac{[CO] \times [H_2O]}{[H_2] \times [CO_2]},$$

where [CO], [H_2O], [H_2], and CO_2 represent the concentrations of CO, H_2O, H_2 and CO_2 at the corresponding temperature.
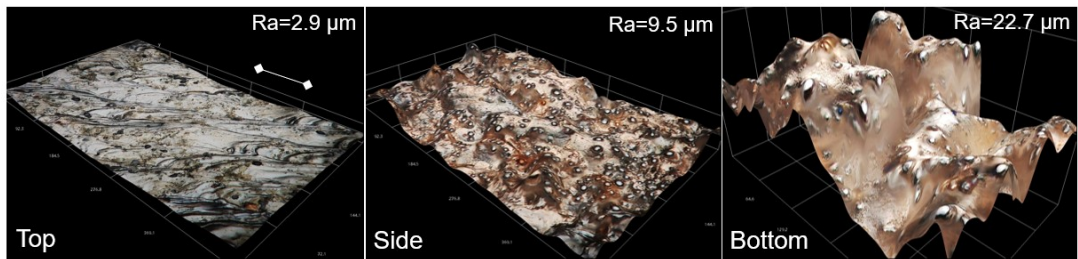
**Fig. S1**. Different cross-section (CS) images from XY, ZY and ZX slicing planes for various catalysts.

Fig. S2. Characterization of the mixing degree of Cu and Ni powders. (a) SEM image

and (b) EDS mapping of Cu and Ni powders after mixture by ball milling.

Fig. S3. Roughness of the as-printed DL2-RD20 catalysts. (a) Top surface, (b) side surface and (c) downside surface studied under the RH-200 high-resolution 3D optical microscope. Scale bar: 92 μm.
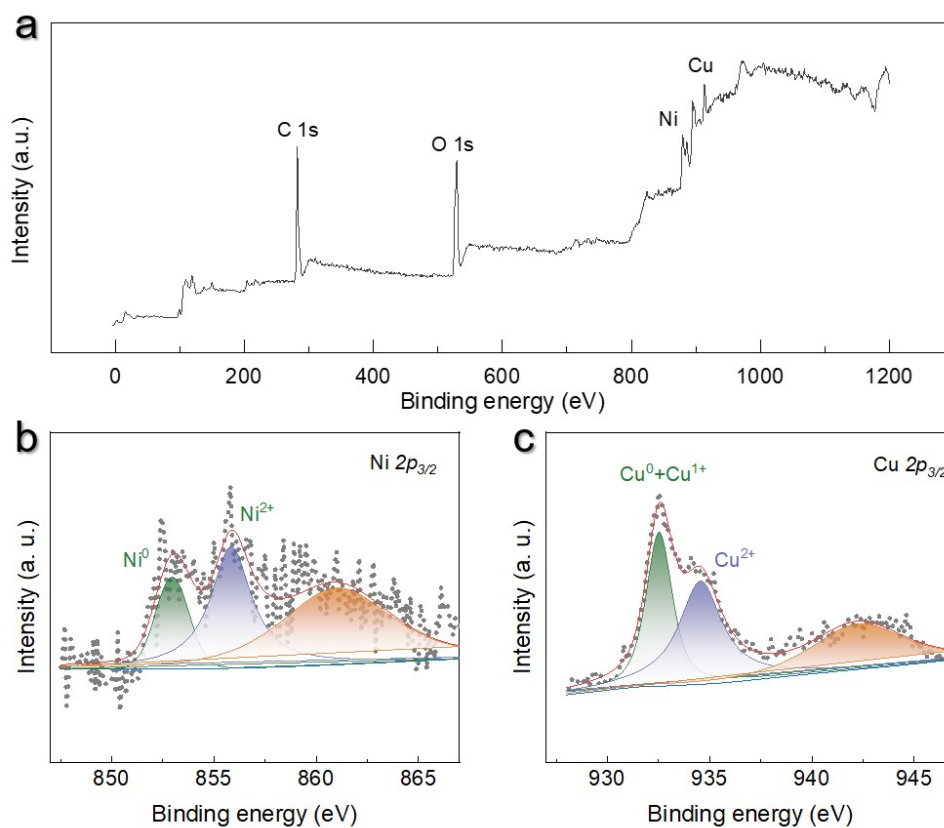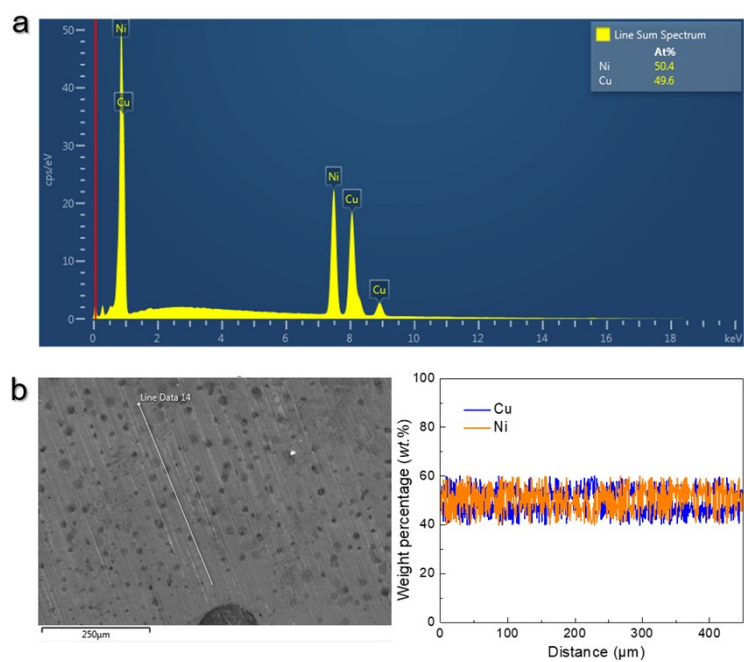

Fig. S4. (a) X-ray photoelectron spectroscopy (XPS) analysis of the as-printed DL2-RD20 catalysts. The XPS analysis of the (b) Ni *2p* and (c) Cu *2p* peaks of the as-printed DL2-RD20 catalysts.
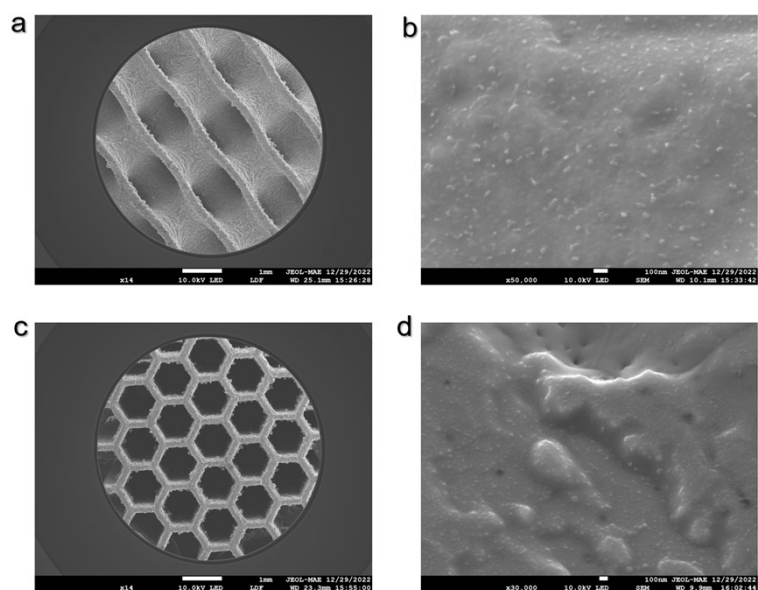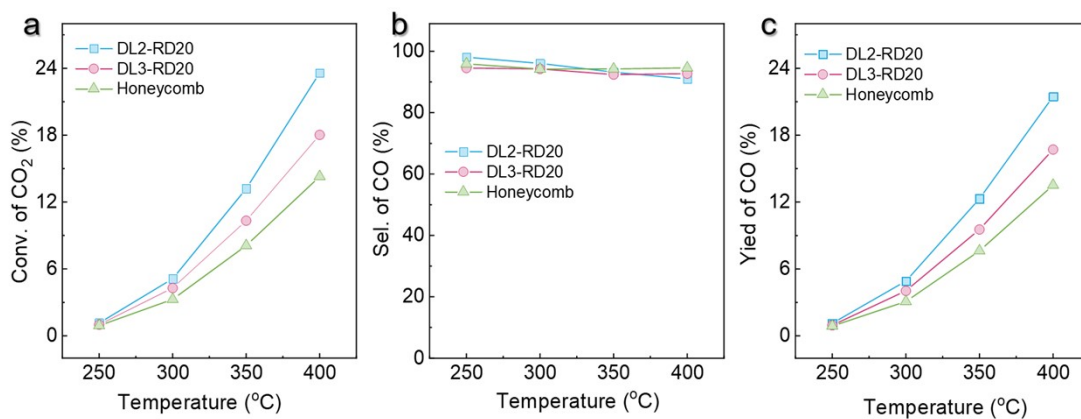
Fig. S5. SEM images of the DL3-DR20 catalyst with (a) low and (b) high magnifications.

STEM images of the honeycomb catalyst with (c) low and (d) high magnifications.

Fig. S6. Element distribution of Cu and Ni on the as-printed sample. (a) EDS analysis of

DL2-RD20. (b) EDS line scan analysis of DL2-RD20.

Fig. S7. Catalytic performance of RWGS reaction by various catalysts. (a) CO_2 conversion, (b) CO selectivity and (c) CO yield as a function of temperature.
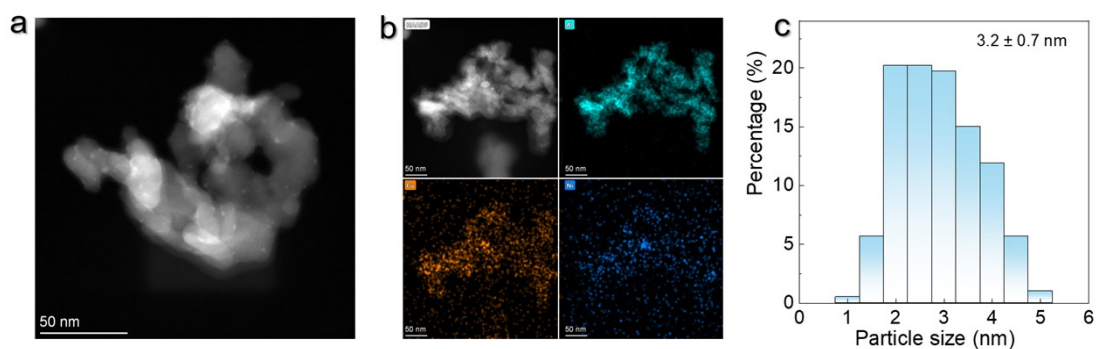
Fig. S8. Characterization of the CuNi/Al_2O_3 catalysts. (a) Dark-field TEM image and (b) EDS mapping of the CuNi/Al_2O_3 catalysts. (c) Size distribution of CuNi nanoparticles for the CuNi/Al_2O_3 catalysts.
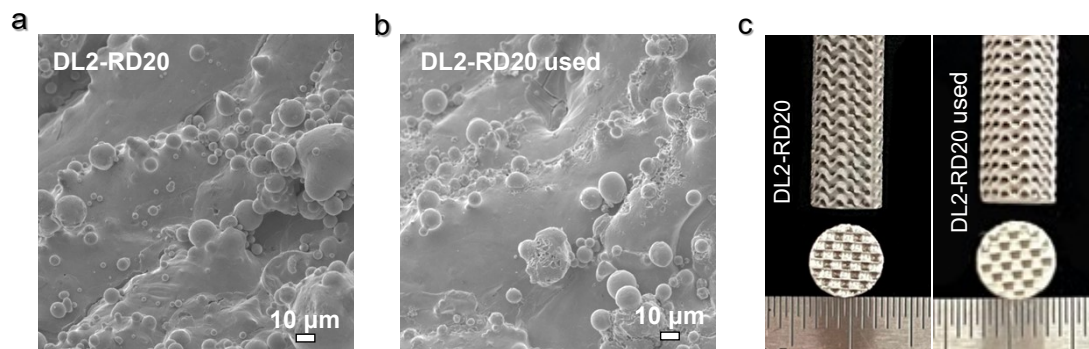
Fig. S9. Characterization of the used DL2-RD20 catalysts. SEM images of (a) the DL2-RD20 catalyst and (b) the used DL2-RD20 catalysts. (c) Picture of the DL2-RD20 catalyst and used DL2-RD20 catalyst.

Table S1. Summary of the catalytic performance of RWGS reaction.

Catalysts	Temp. (°C)	WHSV (mL g^{-1} h^{-1})	CO$_2$ Conv. (%)	CO Sel. (%)	CO formation rate (mmol$_{CO}$ g$_{cat}^{-1}$ h^{-1})	TOF (min^{-1})	Ref.
DL2-RD20	500	1715	59.4	97.8	10.8	276.0	This work
2.4-Ni/nSiO$_2$	500	/	52.0	92.0	17.2	22.9	2
13.9-NiCuSap	500	15,000	52	85.0	71.9	8.3	3
14.9-NiCoSap	500	15,000	49	37.0	24.3	2.6	3
15.1-Ni$_2$P/CeO$_2$	500	300,000	25	62.0	10.1	1.9	4
15.1-Ni/CeO$_2$	500	300,000	22	82.0	9.0	0.06	4
5.9-Ni@S16C	500	/	20	93.0	8.7	0.41	5
Ni-SAs/N-CNTs	500	12,000	64	99.0	41.8	183.2	6
5Ni/Ce-Zr-O	550	30,000	33	54.0	119.3	2.3	7
Ni-1Mo	400	50,000	30	95.0	63.3	1.2	8
7Ni-ZnO-S3	500	30,000	40	98.0	131.2	1.8	9
Ni-0.3Ag/SiO$_2$	400	/	6.0	99.8	49.3	1.2	10
Ni-0.1Ag/SiO$_2$	400	/	4.8	91.0	24.3	1.1	10
Ni-Ga$_2$O$_3$/Al$_2$O$_3$	450	30,000	38.0	98.0	49.8	1.8	11
CuNi-La$_2$O$_3$	500	30,000	62.0	90.0	14.9	1.5	12
Ni-La$_2$O$_3$	500	30,000	48.0	65.0	8.35	0.82	12

Table S2. Summary of the mechanical performance of 3D printed CuNi alloy and reported structures.

Sample	Compressive strain	Specific strength $(MPa\ g^{-1}\ cm^3)$	Ref.
C-microlattice	0.02	25	13
Ceramic-lattice	0.02	28.4	14
	0.05	57.9	
Au-nanolattice	0.8	1.6	15
	0.7	4.6	
Ag-nanolattice	0.48	0.84	16
	0.48	0.55	
Porous Cu	0.6	4.69	17
Coated Porous Cu	0.6	6.01	
Nanoporous Cu	0.018	2.88	18
SiC@SiO$_2$	0.9	4.6	19
CNT@SiO$_2$	0.8	1.16	20
DL2-RD20 CuNi alloy	0.6	19.4	Current work
	0.58	19.1	
	0.56	38.8	
	0.47	17.5	

Reference:

1   Al-Ketan O., Abu Al-Rub R. K. Multifunctional mechanical metamaterials based on triply periodic minimal surface lattices, *Adv. Eng. Mater.*, 2019, **21**, 1900524.

2   R. V. Gonçalves, L. L. R. Vono, R. Wojcieszak, C. S. B. Dias, H. Wender, E. Teixeira-Neto and L. M. Rossi, *Appl. Catal. B Environ.*, 2017, **209**, 240–246.

3   N. Nityashree, C. A. H. Price, L. Pastor-Perez, G. V. Manohara, S. Garcia, M. M. Maroto-Valer and T. R. Reina, *Appl. Catal. B Environ.*, 2020, **261**, 118241.

4   S. Cui, X. Wang, L. Wang and X. Zheng, *Dalton Trans.*, 2021, **50**, 5978–5987.

5   C.-S. Chen, C. S. Budi, H.-C. Wu, D. Saikia and H.-M. Kao, *ACS Catal.*, 2017, **7**, 8367–8381.

6   D. Wang, Z. Yuan, X. Wu, W. Xiong, J. Ding, Z. Zhang and W. Huang, *ACS Catal.*, 2023, **13**, 7132–7138.

7   F. Sun, C. Yan, Z. Wang, C. Guo and S. Huang, *Int. J. Hydrog. Energy*, 2015, **40**, 15985–15993.

8   R. Zhang, A. Wei, M. Zhu, X. Wu, H. Wang, X. Zhu and Q. Ge, *J. CO_2 Util.*, 2021, **52**, 101678.

9   Z. Zhang, Y. Shu, Q. Liu, S. Bi and P. Zhang, *Chem. Eng. J.*, 2023, **475**, 146333.

10 C. Zhang, R. Zhang, Y. Liu, X. Wu, H. Wang, Q. Ge and X. Zhu, *ChemCatChem*, 2023, **15**,e202201284.

11 J. Gong, M. Chu, W. Guan, Y. Liu, Q. Zhong, M. Cao and Y. Xu, *Ind. Eng. Chem. Res.*, 2021, **60**, 9448–9455.

12 P. Ebrahimi, A. Kumar and M. Khraisheh, *Int. J. Hydrog. Energy*, 2023, **48**, 24580–24593.

13 A. Kudo, K. Kanamaru, J. Han, R. Tang, K. Kisu, T. Yoshii, S. Orimo, H. Nishihara and M. Chen, *Small*, 2023, 2301525.

14 R. Wang, H. Ye, J. Cheng, H. Li, P. Zhu, B. Li, R. Fan, J. Chen, Y. Lu and Q. Ge, *Addit. Manuf.*, 2023, **61**, 103361.

15 H. Cheng, X. Zhu, X. Cheng, P. Cai, J. Liu, H. Yao, L. Zhang and J. Duan, *Nat. Commun.*, 2023, **14**, 1243.

16 M. S. Saleh, C. Hu and R. Panat, *Sci. Adv.*, 2017, **3**, e1601986.

17 H. Du, C. Cui, H. Liu, G. Song and T. Xiong, *J Mater. Sci. Technol.*, 2020, **37**, 114–122.

18 Y. Gao, Q. Zhu, Z. Huang, S. Zhang, Y. Wang, G. lv, H. Li, X. Zhang, Z. Hou and H. Zhang, *Chem. Eng. J.*, 2023, DOI: 10.1016/j.cej.2023.146902.

19 L. Su, H. Wang, M. Niu, S. Dai, Z. Cai, B. Yang, H. Huyan and X. Pan, *Sci. Adv.*, 2020, **6**, eaay6689.

20 X. Dong, L. Cao, Y. Si, B. Ding and H. Deng, *Adv. Mater.*, 2020, **32**, 1908269.